Inorganic Chemistry

pubs.acs.org/IC Article

Acetate-Decorated Tri-Ln(III)-Containing Antimonotungstates with a Tetrahedral {WO_4} Group as a Structure-Directing Template and Their Luminescence Properties

Xin Xu, Ruru Meng, Changtong Lu, Ling Mei, Lijuan Chen,* and Junwei Zhao*

Cite This: *Inorg. Chem.* 2020, 59, 3954−3963 Read Online

ACCESS | Metrics & More | Article Recommendations | Supporting Information

ABSTRACT: Four acetate-decorated tri-Ln-substituted trimeric antimonotungstates (AMTs) $Na_{17}\{(WO_4)[Ln(H_2O)(Ac)(B\text{-}\alpha\text{-}SbW_9O_{31}(OH)_2)]_3\}\cdot 50H_2O$ [Ln = Eu^{3+} (**1**), Dy^{3+} (**2**), Ho^{3+} (**3**), or Gd^{3+} (**4**)] were isolated by reaction of $Na_9[B\text{-}\alpha\text{-}SbW_9O_{33}]\cdot 19.5H_2O$, $Na_2WO_4\cdot 2H_2O$, and $Ln(NO_3)\cdot 6H_2O$ in a HAc/NaAc buffer solution. Interestingly, a tetrahedral {WO_4} group plays a significant structure-directing template role in the formation of their polyoxoanions. With regard to luminescence properties, with a change in the excitation wavelength, it is available to switch emission colors from orange to red for **1**, blue to green for **2**, and blue to yellow for **3**. Under the O → W LMCT excitation, energy transfer from AMT fragments to Eu^{3+}, Dy^{3+}, and Ho^{3+} ions occurs because Ln^{3+} ions can absorb energy from O → W LMCT emission of AMT segments. The temperature-dependent luminescence behaviors (25−720 °C) of **1** together with auxiliary emitting photographs illustrate that the growing emission in the temperature range of 25−100 °C results from the loss of lattice water molecules, the decline of emission between 100 and 320 °C may occur because crystals become amorphous powders, the slow emission decay (220−320 °C) is due to the case that the emission enhancement derived from the removal of water ligands on Eu^{3+} ions in some degree compensates for the decline of emission intensity, the sharp decrease in emission (320−520 °C) may result from the change in the coordinate environment of Eu^{3+} ions, and the weak recovery of emission (620−720 °C) may be ascribed to the formation of new phase $Na_{0.5}Eu_{0.5}WO_4$. This work lays a significant foundation for preparing novel POM-based luminescent materials.

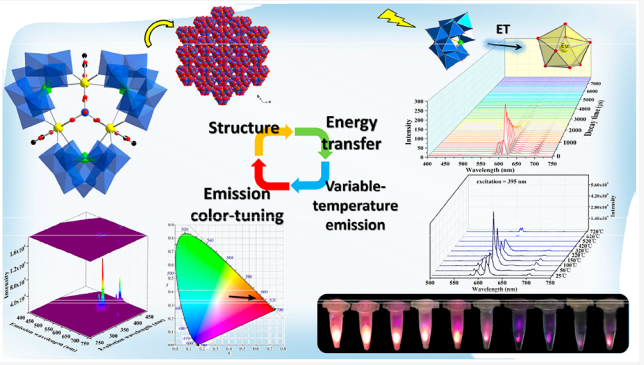

INTRODUCTION

Polyoxometalates (POMs) make up a famous family of polynuclear high-oxidation-state early transition-metal (TM) clusters, which are used in various technical applications such as energy, nonlinear optics, magnetic, catalysis, and sensing.[1−7] Therein, because of the well-established building block strategy that uses preformed lacunary POM precursors to construct novel polyoxotungstate (POT) clusters, considerable attention has been paid to lacunary POTs such as $[XW_9O_{33}]^{9-}$ (X = Sb^{III}, Bi^{III}, or As^{III}) with lone pair electrons on the top of trigonal-pyramid heteroatoms.[8−13] It is worth noting that lacunary POTs as superior multidentate inorganic ligands have the capability to be self-polymerized to stable and giant aggregates, which is attributed to the good structural stability, high surface negative charge, flexible assembly modes, and high affinity for TM or lanthanide (Ln) ions.[14−18] Therefore, lacunary POTs, especially trivacant Keggin-type POTs, allow greater control for the assembly of high-nuclear TM- or Ln-substituted POT materials.[19−22]

For the designed synthesis of novel POT materials, some assembly strategies have been reported, among which the structure-directing template strategy has attracted the interest of researchers in recent years, which can significantly direct the formation of poly(POT) structures.[23] For instance, Cronin et al. prepared a series of ring thiooxomolybdates by virtue of $[Mo_2S_2O_2(H_2O)_6]^{2+}$ and templating squarate dianions.[24] Long and colleagues found that anionic template agents such as CO_3^{2-} and PO_4^{3-} can play an important role in the assembly process.[25] Kortz's group reported a tri-Y-substituted AMT with a {WO_4} tetrahedron as a template.[26] Niu and partners utilized TeO_3^{2-} as a template and linker to obtain two organic−inorganic hybrid POTs (OIHPOTs).[27] Yang and co-workers made a TM-containing OIHPOT comprising a templating four-coordinate {WO_4} group.[28] Thus, the continuous application of this feasible assembly strategy of combining

Received: December 12, 2019
Published: February 24, 2020

trivacant POM precursors with small templates is still a great challenge for the synthesis of novel POT clusters.

In the family of OIHPOTs, the research on Ln-containing organic−inorganic hybrid AMTs (Ln-OIHAMTs) based on trivacant $[B\text{-}\alpha\text{-}SbW_9O_{33}]^{9-}$ fragments is still in its initial stage.[29−32] Previous studies have demonstrated that Ln centers bear high coordination numbers, flexible coordination modes, strong oxophilicity, and obvious coordinate selectivity to O atoms, which can easily bond with carboxylic ligands.[33−36] In turn, carboxylic ligands can induce aggregation of variable metal centers in aqueous solution and stabilize the structures of products through decorating polyoxoanions (POAs) to increase spatial utilization.[37−39]

Ln ions such as Eu^{3+}, Dy^{3+}, Ho^{3+}, Er^{3+}, Tb^{3+}, and Sm^{3+} ions can provide POT materials with admirable luminescence (LS) properties such as sharp emission peaks, large Stokes shifts, and long decay lifetimes.[40,41] POT fragments generally act light-harvesting antennae to sensitize LS emissions of Ln centers through energy transfer (ET) under the O → W ligand-to-metal transfer (LMCT) excitation.[42] Thus, Ln-OIHPOTs will be widely suggested for optic technologies such as white light-emitting diodes (W-LEDs), photodynamic therapy, electroluminescent materials, temperature-dependent imaging, etc.[43,44] For instance, in 2011, Boskovic's group researched the LS sensitization of organic ligands and inorganic POT segments to Eu^{3+} and Tb^{3+} ions.[45] In 2018, Niu et al. studied the LS stability and emission color-tunable properties for W-LEDs by synthesizing a series of Dy^{3+}/Er^{3+}-doped Ln-OIHPOT materials.[46] Nevertheless, variable-temperature LS properties have rarely been reported for Ln-OIHPOT systems. It is also noteworthy that the O−H oscillators in water ligands of Ln ions generally lead to LS quenching of Ln ions, which may originate from ET from Ln ions to O−H vibrational overtones.[47] In addition, some Ln ions are very sensitive to the high-symmetry coordination environment that can result in LS inactivation of Ln ions to some degree.[48,49] Therefore, it is necessary to analyze the relationship between LS and temperature in Ln-OIHPOT systems, illustrating how to design and synthesize temperature-controlling Ln-OIHPOT optic materials by virtue of the correlation between structure and composition.

Inspired by the considerations mentioned above, we prepared four acetate-decorated tri-Ln-substituted trimeric AMTs $Na_{17}\{(WO_4)[Ln(H_2O)(Ac)(B\text{-}\alpha\text{-}SbW_9O_{31}(OH)_2)]_3\}\cdot 50H_2O$ [Ln = Eu^{3+} (**1**), Dy^{3+} (**2**), Ho^{3+} (**3**), or Gd^{3+} (**4**)]. In the assembly of **1**−**4**, extra $Na_2WO_4\cdot 2H_2O$ was added for the generation of the tetrahedral $\{WO_4\}$ group (Figure S1). Apparently, the $\{WO_4\}$ group plays a significant role as a structure-directing template in the formation of POAs. In the case of LS properties, with a change in the excitation wavelength, the emission color-tunable properties for **1**−**3** can be realized. ET processes from AMT fragments to Eu^{3+}, Dy^{3+}, and Ho^{3+} ions have been discussed under O → W LMCT excitation. Variable-temperature LS emission behaviors of **1** have been analyzed in depth.

RESULTS AND DISCUSSION

Structure. Crystallographic data of **1**−**4** are listed in Table S1. The experimental PXRD patterns of **1**−**4** coincide with their simulative XRD patterns, which indicate that these samples are pure (Figure S2). **1**−**4** are isomorphic and crystallize in trigonal space group R_{3m}. Thus, only the structure of **1** is discussed. Bond valence sum (BVS) calculation results illustrate that the oxidation states of all W, Sb, and Eu centers in the POA of **1** are +6, +3, and +3, respectively, and the O4 atom is monoprotonated (Table S2). The molecular unit of **1** comprises an acetate-decorated tri-Eu-substituted $\{(WO_4)[Eu(H_2O)(Ac)(B\text{-}\alpha\text{-}SbW_9O_{31}(OH)_2)]_3\}^{17-}$ (**1a**) trimeric POA, 17 Na^+ cations, and 50 lattice waters. **1a** is composed of three trivacant Keggin-type $[B\text{-}\alpha\text{-}SbW_9O_{33}]^{9-}$ ($\{SbW_9\}$) segments encapsulating a tri-Eu^{3+}-containing $\{(WO_4)[Eu(H_2O)(Ac)]_3\}^{4+}$ (**1b**) cluster connected by 12 μ_2-O atoms (Figure 1a). Three Sb heteroatoms (i.e., Sb1, Sb1A, and Sb1B) in three

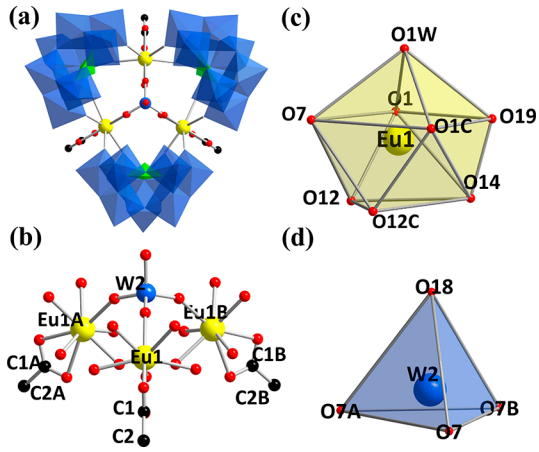

Figure 1. (a) View of **1a**. (b) Ball-and-stick view of **1b**. (c) Coordination geometry of $Eu1^{3+}$. (d) Tetrahedral $\{WO_4\}$ group. Legend: $\{WO_6\}$, mazarine octahedra; $\{WO_4\}$, mazarine tetrahedron; O, red spheres; W, mazarine spheres; Sb, green spheres; Eu, bright yellow spheres; C, black spheres. Symmetry code: A, $1 - x + y$, $2 - x$, z; B, $2 - y$, $1 + x - y$, z; C: x, $x - y$, z.

$\{SbW_9\}$ segments exhibit an equilateral triangle distribution and are situated on three vertices of a triangle (Sb···Sb, 7.665 Å) (Figure S3a). **1b** consists of three $[Eu1(H_2O)]^{3+}$ ions, three acetate groups, and a capping tetrahedral $\{WO_4\}$ group (Figure 1b). Therein, three crystallographically equivalent Eu^{3+} ions (i.e., Eu1, Eu1A, and Eu1B) in **1b** are also aligned in an equilateral triangle mode (Eu···Eu, 5.889 Å) (Figure S3b). The $Eu1^{3+}$ ion exhibits an octacoordinate distorted monocapped square antiprismatic configuration established by four μ_2-O atoms from two $\{SbW_9\}$ segments [Eu1−O1, 2.388(11) Å; Eu1−O12, 2.407(12) Å; Eu1−O1C, 2.388(11) Å; Eu1−O12C, 2.407(12) Å], two carboxyl O atoms [Eu1−O14, 2.465(18) Å; Eu1−O19, 2.519(18) Å], one μ_2-O atom from the capping tetrahedral $\{WO_4\}$ subunit [Eu1−O7, 2.346(17) Å], and one aqua ligand [Eu1−O1W, 2.354(19) Å] (Figure 1c). Compared to the previous reports, the capping tetrahedral $\{WO_4\}$ group is rare because it is different from the hexacoordinate $\{WO_6\}$ octahedra.[26] The tetrahedral $\{WO_4\}$ group is situated on the center of the POA. Three bridging O atoms (i.e., O7, O7A, and O7B) of the tetrahedral $\{WO_4\}$ group show an equilateral triangle mode and cooperate with the terminal O18 atom to establish a tetrahedron (Figure 1d). It can be considered that the equilateral triangle mode formed by O7, O7A, and O7B induces the formation of the equilateral triangle distribution of three $Eu1^{3+}$ ions (Figure S4), to further drive the arrangement of three $\{SbW_9\}$ segments (Figure S5). Therefore, the tetrahedral $\{WO_4\}$ group plays a significant structure-directing templating role in the formation of **1a**.

https://dx.doi.org/10.1021/acs.inorgchem.9b03620
Inorg. Chem. 2020, 59, 3954−3963

Three terminal acetate groups are connected with three Eu^{3+} ions, which increases space utilization.

Furthermore, three-dimensional (3D) supramolecular architecture of **1a** shows a beautiful stacking pattern. Viewed along the *c* axis, each **1a** is surrounded by six **1a** molecules, and six **1a** molecules exhibit a hexagonal alignment and are located on the six vertices of the hexagon (Figure 2a and Figure S6a).

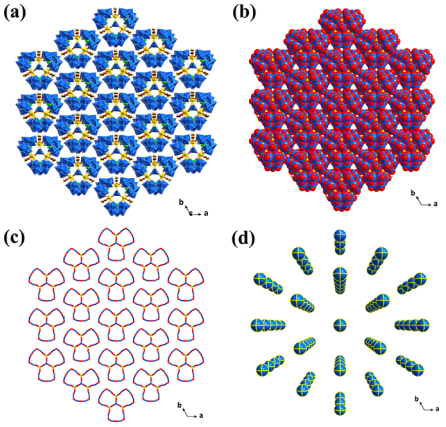

Figure 2. (a) Polyhedral and (b) space-filling views of the 3D stacking for **1a** along the *c* axis. (c and d) Simplified 3D stacking representations for **1a** along the *c* axis.

Furthermore, the hexagonal geometry is further surrounded by 12 **1a** molecules, which form a larger hexagonal geometry (Figure 2b–d). Therefore, it can be inferred that the epitaxial alignment of **1a** effectively influences the formation of hexagonal crystals along the *c* axis. Along the direction of the *a* axis, these hexagonal geometries are parallel and the angle formed by the hexagonal geometries and *c* axis is approximately 60.0° (Figure S6b–d).

LS Studies. Previous research demonstrates that emission colors of Ln-AMTs can be tuned through switching variable excitation lights, which can realize the emission-tunable property.[50,51] In addition, W–O–Ln bond angles near 150° will result in dπ–pπ–fπ orbital mixing, which can lead to inactivity of ET from AMT segments to Ln^{3+} ions. Fortunately, no W–O–Ln bond angles near 150° in **1**–**3** have been found, which suggests that ET cannot be inhibited by dπ–pπ–fπ orbital mixing.[52−54] In this work, excitation and emission spectra, decay lifetime curves, and time-resolved emission spectra (TRES) as measurement methods have been measured to analyze the PL properties of **1**–**3**.

Upon ultraviolet (UV) excitation of Eu^{3+} (λ_{ex} = 395 nm), **1** gives out five Eu^{3+} characteristic emissions at 580, 595, 613, 651, and 701 nm, which are assigned to the $^5D_0 \rightarrow {}^7F_J$ (J = 0, 1, 2, 3, and 4, respectively) transitions (Figure 3a). Therein, the electronic $^5D_0 \rightarrow {}^7F_2$ transition of Eu^{3+} ions is highly sensitive to the coordination environment with no inversion symmetry, while the magnetic dipole $^5D_0 \rightarrow {}^7F_1$ transition is not sensitive with an inversion symmetry. The intensity ratio of $^5D_0 \rightarrow {}^7F_2$ and $^5D_0 \rightarrow {}^7F_1$ transitions can be used to explore the local environment of Eu^{3+} ions. The $I(^5D_0 \rightarrow {}^7F_2)/I(^5D_0 \rightarrow {}^7F_1)$ intensity ratio of 3.33 for **1** illustrates that Eu^{3+} ions reside in a low-symmetry microenvironment.[55−58] The excitation spectrum of **1** measured by monitoring the maximum emission peak at 613 nm presents a wide O → W LMCT band (LMCTB) centered at ∼314 nm that can be attributed to the $^1T_{1u} \leftarrow {}^1A_{1g}$ transition originating from O → W LMCT triplet states of AMT segments, and six f–f excitation peaks at 364, 383, 395, 416, 465, and 540 nm, assigned to Eu^{3+} $^5D_4 \leftarrow {}^7F_0$, $^5L_7 \leftarrow {}^7F_0$, $^5L_6 \leftarrow {}^7F_0$, $^5D_3 \leftarrow {}^7F_0$, $^5D_2 \leftarrow {}^7F_0$, and $^5D_1 \leftarrow {}^7F_0$ transitions, in which the peak at 395 nm is the most intense excitation peak (Figure S7a).[59] The decay lifetime curve of **1** based on monitoring the strongest emission at 613 nm abides by the monoexponential equation [$I = I_0 \exp(-t/\tau)$], affording a τ of 835.28 ± 1.79 μs (Figure S7b and Table S3).[60] In **2**, upon the most intensive f–f $^4I_{15/2} \leftarrow {}^6H_{15/2}$ excitation of Dy^{3+} at 455 nm, the emission spectrum presents three emission peaks at 484, 575, and 662 nm corresponding to Dy^{3+} f–f $^4F_{9/2} \rightarrow {}^6H_K$ (K = 15/2, 13/2, and 11/2) transitions (Figure S8a). When the 575 nm emission is monitored, the obtained excitation spectrum shows a broad O → W LMCTB ($^1T_{1u} \leftarrow {}^1A_{1g}$) at 272 nm derived from AMT segments, and a series of excitation peaks at 353, 365, 389, 426, and 455 nm ascribed to Dy^{3+} $^6P_{7/2} \leftarrow {}^6H_{15/2}$, $^6P_{5/2} \leftarrow {}^6H_{15/2}$, $^4I_{13/2} \leftarrow {}^6H_{15/2}$, $^4G_{11/2} \leftarrow {}^6H_{15/2}$, and $^4I_{15/2} \leftarrow {}^6H_{15/2}$ transitions (Figure S8b).[61,62] The decay lifetimes of **2** according to the second-order exponential equation [$I = A_1 \exp(-t/\tau_1) + A_2 \exp(-t/\tau_2)$] and the average lifetime function [$\tau^* = (A_1\tau_1^2 + A_2\tau_2^2)/(A_1\tau_1 + A_2\tau_2)$] demonstrate that the correlative τ_1, τ_2, and τ^* are 3.56 ± 0.03, 10.92 ± 0.28, and 5.82 μs, respectively (Figure S8c and Table S3), where the short and long lifetimes (τ_1 and τ_2) are ascribed to the LS contributions of AMT fragments and Dy^{3+} ions, respectively. When **3** was excited on the basis of the Ho^{3+} f–f $^5G_6 \leftarrow {}^5I_8$ transition at 452 nm, **3** generates a weak emission peak at 557 nm ($^5F_4 + {}^5S_2 \rightarrow {}^5I_8$ of Ho^{3+} ions) and a strong emission peak at 660 nm ($^5F_5 \rightarrow {}^5I_8$ of Ho^{3+} ions); when the emission at 660 nm was monitored (Figure S8d), the excitation spectrum shows an O → W LMCTB ($^1T_{1u} \leftarrow {}^1A_{1g}$) at 260 nm and two Ho^{3+} f–f excited peaks at 419 ($^5G_5 \leftarrow {}^5I_8$) and 452 nm ($^5G_6 \leftarrow {}^5I_8$) (Figure S8e).[63,64] By virtue of the second-order exponential equation and average lifetime formula, and the corresponding decay lifetimes of **3** determined by monitoring the most powerful emission at 660 nm, τ_1, τ_2, and τ^* are 1172.53 ± 13.13, 9180.30 ± 205.90, and 5370.65 ns, respectively (Figure S8f and Table S3), in which the short and long lifetimes (τ_1 and τ_2, respectively) derive from the LS contributions of AMT fragments and Ho^{3+} ions.

The presence of O → W LMCTBs in excitation spectra of **1**–**3** implies that AMT fragments can absorb light energy to prompt the luminescence of Eu^{3+}, Dy^{3+}, and Ho^{3+} ions. Therefore, the AMT fragment can act as the light-harvesting antennae to transfer energy to Eu^{3+}, Dy^{3+}, and Ho^{3+} ions in **1**–**3** upon photoexcitation of O → W LMCT triplet states. Under O → W LMCT excitation of AMT fragments (λ_{ex} = 268 nm), **4** gives a $^3T_{1u} \rightarrow {}^1A_{1g}$ emission band (350–600 nm) of AT fragments (Figure S9).

To investigate the ET process from AMT fragments to Eu^{3+}, Dy^{3+}, and Ho^{3+} ions in **1**–**3**, the overlap between the excitation peaks of Eu^{3+}, Dy^{3+}, and Ho^{3+} ions and the $^3T_{1u} \rightarrow {}^1A_{1g}$ emission band of AMT fragments of **4** has been depicted (Figure 3b and Figure S10a,b), which indicates that AMT fragments can transfer energy to Eu^{3+}, Dy^{3+}, and Ho^{3+} ions in the form of energy re-absorption in **1**–**3**. As one can clearly see in Figure S10c, under the O → W LMCT excitation of **1** (λ_{ex} = 314 nm), emission spectrum of **1** in the range of 400–700 nm exhibits the f–f emissions mentioned above at 580, 595, 613, 651, and 701 nm, which can be assigned to the $^5D_0 \rightarrow {}^7F_J$ (J = 0, 1, 2, 3, or 4) transitions of Eu^{3+} ions. The absence of the

https://dx.doi.org/10.1021/acs.inorgchem.9b03620
Inorg. Chem. 2020, 59, 3954−3963

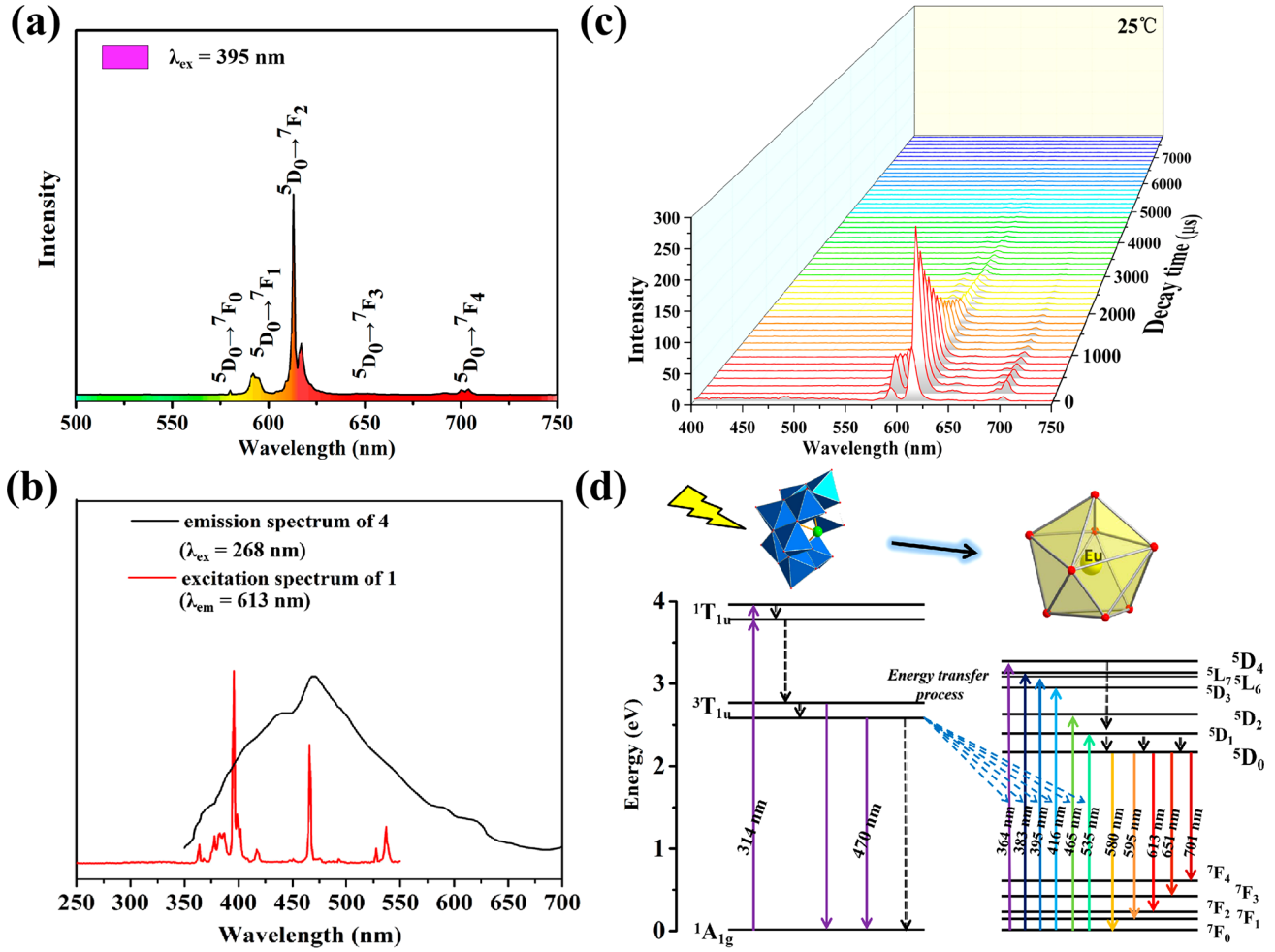

Figure 3. (a) Emission spectrum of **1** with a λ_{ex} of 395 nm. (b) Overlap between the excitation spectrum of **1** and the $^3T_{1u} \rightarrow {}^1A_{1g}$ emission band of **4**. (c) TRES spectra of **1** with a λ_{ex} of 314 nm. (d) Schematic energy level diagram of **1** indicating the ET process from AMT fragments to Eu^{3+} ions (the solid line is the radiation transition, and the dotted line is the nonradiative transition).

$^3T_{1u} \rightarrow {}^1A_{1g}$ emission band of AMT fragments can be attributed to the strong LS quenching led by the ET from AMT fragments to Eu^{3+} ions.[65] Under the O → W LMCT excitation of **2** (λ_{ex} = 272 nm), **2** exhibits a wide $^3T_{1u} \rightarrow {}^1A_{1g}$ emission band (~400−480 nm) and three f−f emission peaks of Dy^{3+} ions at 484, 575, and 662 nm owing to the f−f $^4F_{9/2} \rightarrow {}^6H_K$ (K = 15/2, 13/2, and 11/2) transitions of Dy^{3+} ions (Figure S10d). Under the O → W LMCT excitation of **3** (λ_{ex} = 272 nm), **3** shows a wide $^3T_{1u} \rightarrow {}^1A_{1g}$ emission band (~400−480 nm) and two weak f−f emission peaks of Ho^{3+} ions at 557 and 660 nm, which derived from the $^5F_4 + {}^5S_2 \rightarrow {}^5I_8$ and $^5F_5 \rightarrow {}^5I_8$ transitions (Figure S10e).

TRES spectra of **1**−**3** were also recorded under O → W LMCT excitation at room temperature to analyze ET with the dependence of emission intensity on time. As depicted in Figure 3c, upon excitation of **1** under excitation at 314 nm, five f−f emission peaks centered at 580, 595, 613, 651, and 701 nm start to increase at 0.00 μs and reach the maximum at 160.0 μs. Thereafter, the intensities of these emission peaks decline rapidly and vanished by 5120 μs. The absence of the broad $^3T_{1u} \rightarrow {}^1A_{1g}$ emission band is also due to ET from AMT fragments to Eu^{3+} ions. TRES of **2** (λ_{ex} = 272 nm) demonstrates that the intensities of the broad $^3T_{1u} \rightarrow {}^1A_{1g}$ emission band (400−480 nm) and three f−f emission peaks at 484, 575, and 662 nm start to increase at 99.8 μs and reach the maximum at 109.8 μs. Thereafter, the intensity of the $^3T_{1u} \rightarrow {}^1A_{1g}$ emission band weakens to vanish at 189.6 μs; however, the intensities of three f−f emission peaks disappear at 399.2 μs (Figure S11a). From the viewpoint of the decay rate of these emissions, the decay rate of $^3T_{1u} \rightarrow {}^1A_{1g}$ emission of AMT fragments is faster than that of f−f emission of Dy^{3+} ions, suggesting that the ET process from AMT fragments to Dy^{3+} ions in some degree inhibits the decay rate of f−f emission of Dy^{3+} ions. TRES of **3** (λ_{ex} = 260 nm) illustrates that intensities of the broad $^3T_{1u} \rightarrow {}^1A_{1g}$ emission band (400−480 nm) and two f−f emission peaks at 557 and 660 nm start to increase at 7.9 μs and reach the maximum at 11.0 μs. Then the $^3T_{1u} \rightarrow {}^1A_{1g}$ emission band and two f−f emission peaks weaken to vanish at 30.0, 19.0, and 13.0 μs, respectively (Figure S12b). From the viewpoint of the decay rate, the decay rate of $^3T_{1u} \rightarrow {}^1A_{1g}$ emission of AMT fragments is faster than that of f−f emission peaks of Ho^{3+}, indicating that the ET process from AMT fragments to Ho^{3+} ions has not inhibited the decay rate of f−f emission of Ho^{3+} ions, but the ET process still can be supported by the overlap of the emission band of AMT fragments and excitation peaks of Ho^{3+} ions (Figure S10b). In accordance with the ET analysis described above, the schematic ET process in **1** is described in Figure 3d. Upon photoexcitation of the O → W LMCT triple state, the electrons jump from the $^1A_{1g}$ ground state to the $^1T_{1u}$ excited

https://dx.doi.org/10.1021/acs.inorgchem.9b03620
Inorg. Chem. 2020, 59, 3954−3963

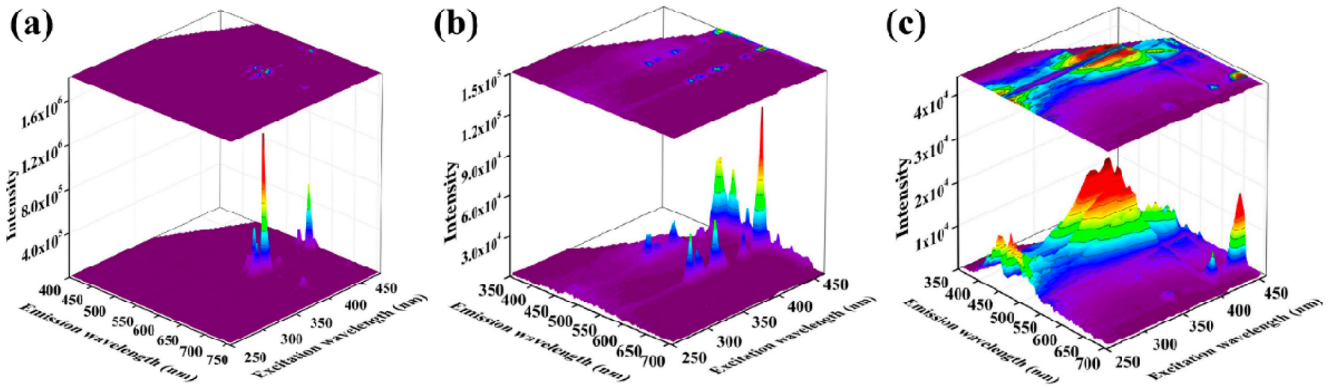

Figure 4. (a) Emission spectra of **1** at different excitation wavelengths (250−470 nm). (b) Emission spectra of **2** at different excitation wavelengths (250−455 nm). (c) Emission spectra of **3** at different excitation wavelengths (250−455 nm).

state and then declined to the $^3T_{1u}$ state in the form of nonradiative relaxation. During the decay process based on the $^3T_{1u} \rightarrow {}^1A_{1g}$ transition, owing to the overlap of the $^3T_{1u} \rightarrow {}^1A_{1g}$ emission band of AMT fragments and the excitation peaks at 364, 383, 395, 416, 465, and 540 nm ($^5D_4 \leftarrow {}^7F_0$, $^5L_7 \leftarrow {}^7F_0$, $^5L_6 \leftarrow {}^7F_0$, $^5D_3 \leftarrow {}^7F_0$, $^5D_2 \leftarrow {}^7F_0$, and $^5D_1 \leftarrow {}^7F_0$ transitions of Eu^{3+}), part of the energy from the $^3T_{1u}$ state of AMT fragments is re-absorbed by these excited transitions of Eu^{3+} in the form of nonradiative relaxation, further prompting the $^5D_0 \rightarrow {}^7F_J$ (J = 0, 1, 2, 3, or 4) emission transitions. The schematic ET process in **2** reveals that during the decay process based on the $^3T_{1u} \rightarrow {}^1A_{1g}$ transition, because of the overlap between the $^3T_{1u} \rightarrow {}^1A_{1g}$ emission band of AMT fragments and the excitation peaks at 353, 365, 389, 426, and 455 nm of Dy^{3+} ions, part of the energy is re-absorbed by $^6P_{7/2} \leftarrow {}^6H_{15/2}$, $^6P_{5/2} \leftarrow {}^6H_{15/2}$, $^6I_{13/2} \leftarrow {}^6H_{15/2}$, $^6G_{11/2} \leftarrow {}^6H_{15/2}$, and $^6I_{15/2} \leftarrow {}^6H_{15/2}$ transitions of Dy^{3+} in the form of nonradiative relaxation, further prompting Dy^{3+} $^4F_{9/2} \rightarrow {}^6H_K$ (K = 15/2, 13/2, and 11/2) emission transitions (Figure S11c). The schematic ET process in **3** shows that during the decay process based on the $^3T_{1u} \rightarrow {}^1A_{1g}$ transition, part of the energy from the $^3T_{1u} \rightarrow {}^1A_{1g}$ transition of AMT fragments is re-absorbed by Ho^{3+} $^5G_5 \leftarrow {}^5I_8$ and $^5G_6 \leftarrow {}^5I_8$ excited transitions in the form of nonradiative relaxation, further prompting Ho^{3+} $^5F_4 + {}^5S_2 \rightarrow {}^5I_8$ and $^5F_5 \rightarrow {}^5I_8$ emission transitions (Figure S11d).

CIE 1931 is conducive to understanding the authenticity of colors. The chromaticity coordinates, dominant wavelength, color purity, and correlated color temperature (CCT) are all significant light optical parameters. Therein, chromaticity coordinates are on behalf of the actual emission color of luminescent materials. The dominant wavelength is the mixed color of the emission spectrum and reference light source. Color purity means the brightness of colors. The low CCTs (<3000 K) will give us warm feelings, and standard CCTs is in the range of 3000−5000 K and the high CCTs (>5000 K) will be cold.[66−68]

To verify the emission color-tunable property, emission spectra have been measured by varying excitation wavelengths from 250 to 470 nm for **1**, from 250 to 455 nm for **2**, and from 250 to 455 nm for **3** (Figure 4). Upon excitation at 395 nm, the emission intensities of five obvious f−f emission peaks at 580, 595, 613, 651, and 701 nm are the most intense, which indicates that the $^5L_6 \leftarrow {}^7F_0$ excitation at 395 nm is the most suitable excitation for **1** (Figure 4a). Upon excitation at 455 nm, the emission intensities of three obvious f−f emission peaks at 484, 575, and 662 nm are the strongest, which indicates that the $^4I_{15/2} \leftarrow {}^6H_{15/2}$ excitation at 455 nm is the most suitable excitation for **2** (Figure 4b). Upon excitation at 452 nm, the emission intensity of the obvious f−f emission peak at 660 nm is the strongest, which suggests that the $^5G_6 \leftarrow {}^5I_8$ excitation at 452 nm is the most suitable excitation for **3** (Figure 4c). Furthermore, their corresponding CIE chromaticity coordinates obtained from the emission spectra under different excitation wavelengths move from (0.360, 0.345) to (0.642, 0.355) for **1**, from (0.240, 0.333) to (0.281, 0.446) for **2**, and (0.174, 0.155) to (0.465, 0.494) for **3** (Tables S4−S6), which illustrates that with a change in excitation wavelength, it is available to switch emission colors from orange to red for **1**, blue to green for **2**, and blue to yellow for **3** (Figure S12a−c).

Color purity can be calculated by the equation color purity = $[(x - x_i)^2 + (y - y_i)^2/(x_d - x_i)^2 + (y_d - y_i)^2]^{1/2}$, where (x, y) is the color coordinate of the light source, (x_i, y_i) is the coordinate of the white light centered at (0.3333, 0.3333), and (x_d, y_d) is the coordinate involving the dominant wavelength. CCT can be calculated through the equation CCT = $499.0n^3 + 3525.0n^2 + 6823.3n + 5520.22$, where $n = (x - x_e)/(y_e - y)$, where x_e (0.3320) and y_e (0.1858) are epicenter coordinates obtained by consecutive tests to minimize the error.[69,70] All data of dominant wavelengths, color purity, and CCTs of **1**−**3** are listed in Tables S4−S6, in which **1** shows the highest color purity of 98.83% (λ_{ex} = 395 nm) compared with **2** and **3**.

Temperature is an important factor influencing the LS emission of Ln-AMTs. To investigate variable-temperature LS properties, excitation, emission, TRES spectra, and auxiliary emitting photographs (Figure 5) of **1** have been measured at different temperatures (25−720 °C) because **1** can show a visible red emission. When the temperature increases from 25 to 100 °C, upon excitation at 395 and 314 nm, the intensity of the emission peak at 613 nm increases to the maximum (Figure 5a,b and Figure S13a,b). When the emission at 613 nm is monitored, excitation spectra exhibit excitation peaks at 395 and 314 nm that also increase to the maximum (Figure 5c,d and Figure S14). TRES spectra measured upon excitation at 314 nm also show that the decay time of the emission peak at 613 nm ceaselessly increases to the maximum (Figures S15 and S16). In summary, the absorption of Eu^{3+} ions and AMT fragments to light can be strengthened when some lattice water molecules are removed, to enhance further the emission intensity and to prolong the emission decay. The reason may be that lattice water molecules can absorb some light energy

https://dx.doi.org/10.1021/acs.inorgchem.9b03620
Inorg. Chem. 2020, 59, 3954−3963

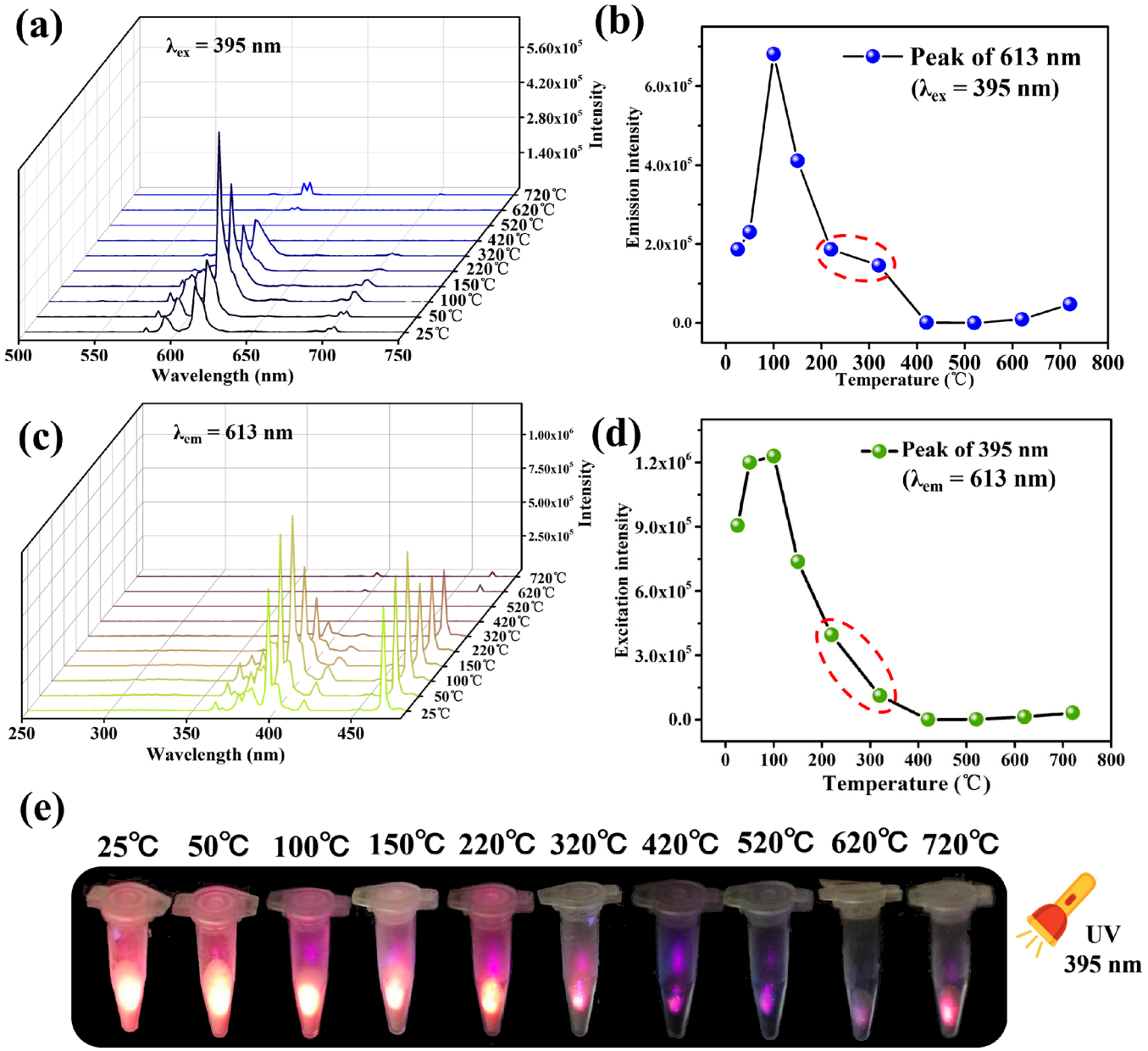

Figure 5. (a) Emission spectra (λ_{ex} = 395 nm) of **1** at different temperatures. (b) Variation of the emission intensity at 613 nm with temperature (λ_{ex} = 395 nm). (c) Excitation spectra (λ_{em} = 613 nm) of **1** at different temperatures. (d) Variation of the excitation intensity at 395 nm with temperature. (e) Emission colors of **1** at different temperatures under a 395 nm xenon lamp (the purple light comes from the xenon lamp at 395 nm).

through thermal vibration, so removal of some lattice water molecules can enhance the light absorption of POA of **1**.[71]

When the temperature further increases from 100 to 320 °C, the intensity of the emission peak at 613 nm (λ_{ex} = 395 and 314 nm) decreases gradually (Figure 5a,b and Figure S13a,b). The excitation intensities of the peaks at 395 and 314 nm also decrease slowly (Figure 5c,d and Figure S14). TRES spectra reveal that the decay time of the emission peak at 613 nm decreases continuously (Table S7 and Figure S16), possibly because the high temperature leads to the removal of lattice and coordinate water molecules, further making crystals become amorphous. The amorphous state of crystals may enhance the light reflective ability, which effectively weakens light absorption of **1**.[72] The decrease in light absorption could coincide well with the decreasing excitation intensities of the peaks at 395 and 314 nm (Figure 5d and Figure S14). The decreasing transparency of crystals seen in Figure 6a shows that the color of the crystal becomes more and more gloomy with an increase in temperature under the incandescent light. The shadow area of the crystal under 395 nm UV light grows gradually with an increase in temperature (from 150 to 320 °C) (Figure 6b). It could be also observed that when temperature increases from 220 to 320 °C, the intensities of excitation peaks at 395 and 314 nm decrease rapidly (Figure 5d and Figure S14), the intensity of the emission peak at 613 nm declines very slowly (Figure 5b and Figure S13b), and the decay rate of the emission peak at 613 nm decreases slowly, which may be caused the fact that the removal of water ligands reduces the quenching effect of luminescence and this can in some degree inhibit the decay of the emission intensity.[47]

https://dx.doi.org/10.1021/acs.inorgchem.9b03620
Inorg. Chem. 2020, 59, 3954−3963

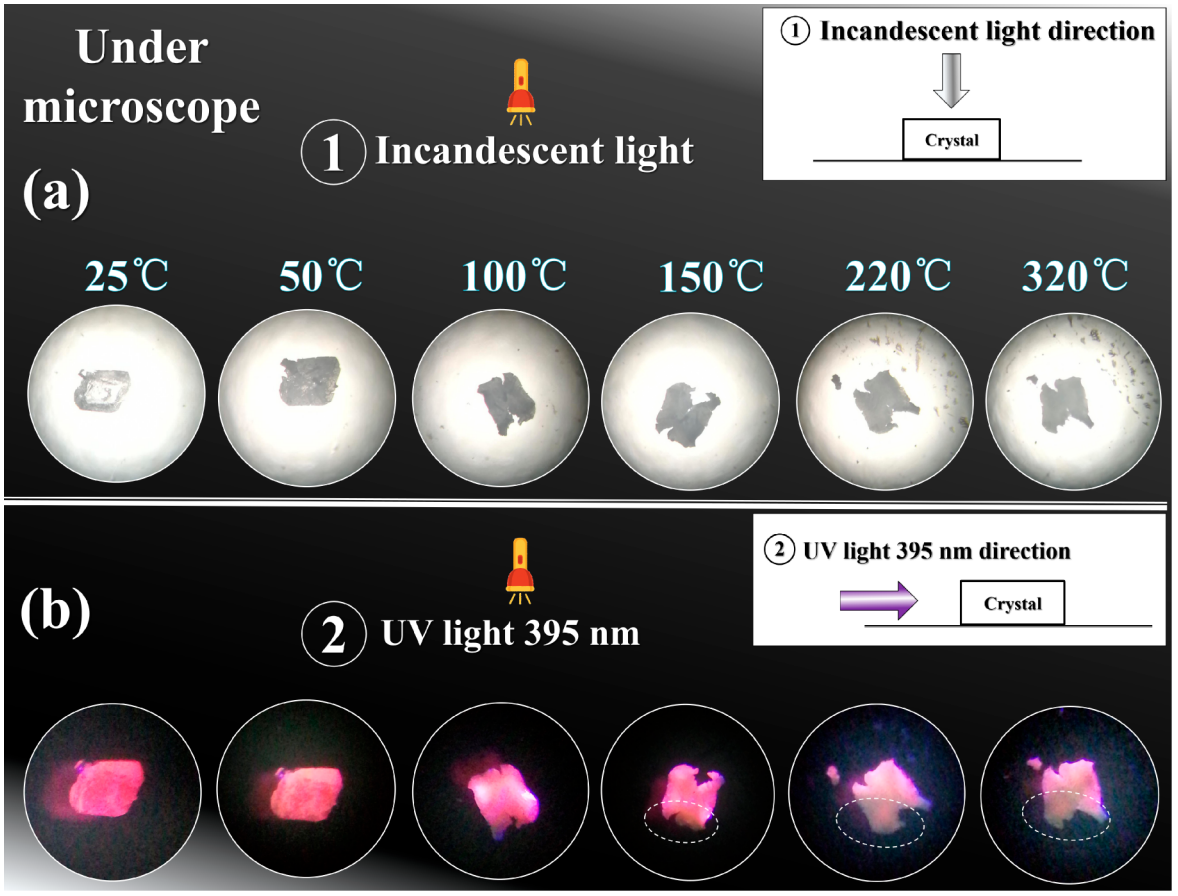

Figure 6. (a) Samples of **1** at different temperatures (25−320 °C) under the incandescent light. (b) Samples of **1** at different temperatures (25−320 °C) under 395 nm UV light.

Fortunately, under 395 and 314 nm UV light, the red emission light of samples obtained at 25−320 °C is still obvious, and the change in emission intensity is in accord with the results of emission spectra (Figure 5e and Figure S13c).

When the temperature increases from 320 to 420 °C, and then to 520 °C, the sharp decrease in the emission intensity (λ_{ex} = 395 and 314 nm) may be derived from the result of the collapse of the polyoxoanion skeleton of **1**, leading to the change in the coordination environments of Eu^{3+} ions (Figure 5b and Figure S13b). As shown in Figure 7, the intensity ratio of $^5D_0 \rightarrow {}^7F_2$ and $^5D_0 \rightarrow {}^7F_1$ transitions of Eu^{3+} declines from 5.80 (320 °C) to 2.97 (420 °C) and then to the minimum of 0.75 (520 °C), which suggests that the coordination environment of Eu^{3+} is greatly changed due to the collapse of the polyoxoanion skeleton. When the temperature further increases to 720 °C, the emission intensity displays a weak recovery because of the formation of a new phase (Figure 5b and Figure S13b). As shown by TRES spectra of **1** measured at 420−720 °C, the emission band ~400−600 nm groups can be observed, which may arise from $\{WO_n\}$ groups or $Na_{0.5}Eu_{0.5}WO_4$ in new phases (Figure S17). The relative $I(^5D_0 \rightarrow {}^7F_2)/I(^5D_0 \rightarrow {}^7F_1)$ value at 720 °C is 9.26, indicating that Eu^{3+} in $Na_{0.5}Eu_{0.5}WO_4$ occupies a low-symmetry environment. Previous literature has shown that the symmetry of Eu^{3+} ions in $Na_{0.5}Gd_{0.5x}Eu_{0.5(1-x)}WO_4$ is low.[73]

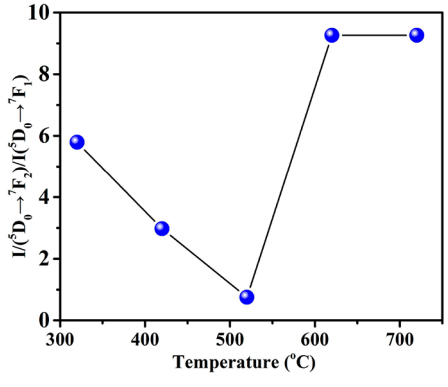

Figure 7. Intensity ratio of $^5D_0 \rightarrow {}^7F_2$ and $^5D_0 \rightarrow {}^7F_1$ transitions at different temperatures based on Figure 5a.

CONCLUSIONS

In summary, four acetate-decorated tri-Ln-substituted trimeric AMTs **1**−**4** were prepared. The tetrahedral $\{WO_4\}$ group can play the important role of a template in the formation of polyoxoanions, which suggests that various $\{WO_n\}$ (n = 4, 5, and 6) units will extend the structure-directing template synthesis strategy for the construction of new-type POT clusters. In addition, under the guidance of the template synthesis strategy, multicarboxylic ligands introduced into the Ln-OIHPOT system will enrich the structural chemistry of POMs. With a variation in the excitation wavelength, changes in emission colors from orange to red for **1**, blue to green for **2**, and blue to yellow for **3** are observed. Under O → W LMCT excitation, the occurrence of ET from AT fragments to Eu^{3+}, Dy^{3+}, and Ho^{3+} ions has been observed. The growing emission

https://dx.doi.org/10.1021/acs.inorgchem.9b03620
Inorg. Chem. 2020, 59, 3954−3963

of **1** in the range of 25−100 °C is led by the loss of lattice water molecules. The decline of emission (100−320 °C) may be caused by the crystal becoming amorphous. The slow emission decay (220−320 °C) of **1** is due to the elimination of water ligands. The sharp decline of emission (320−520 °C) may result from the change in the coordination environment of Eu^{3+} ions. The weak recovery of emission may be ascribed to the formation of new $Na_{0.5}Eu_{0.5}WO_4$. This work not only extends the application of the structure-directing template strategy in synthesizing novel poly(POT) structures but also provides a feasible research method for investigating the variable-temperature luminescence properties of novel POM-based optical materials.

■ ASSOCIATED CONTENT

Supporting Information

The Supporting Information is available free of charge at https://pubs.acs.org/doi/10.1021/acs.inorgchem.9b03620.

Related structural figures, IR spectra and TG curves, and related luminescence spectra and luminescence decay curves (PDF)

Accession Codes

CCDC 1970816−1970819 contain the supplementary crystallographic data for this paper. These data can be obtained free of charge via www.ccdc.cam.ac.uk/data_request/cif, or by emailing data_request@ccdc.cam.ac.uk, or by contacting The Cambridge Crystallographic Data Centre, 12 Union Road, Cambridge CB2 1EZ, UK; fax: +44 1223 336033.

■ AUTHOR INFORMATION

Corresponding Authors

Lijuan Chen − *Henan Key Laboratory of Polyoxometalate Chemistry, College of Chemistry and Chemical Engineering, Henan University, Kaifeng, Henan 475004, China*; Email: ljchen@henu.edu.cn

Junwei Zhao − *Henan Key Laboratory of Polyoxometalate Chemistry, College of Chemistry and Chemical Engineering, Henan University, Kaifeng, Henan 475004, China*; orcid.org/0000-0002-7685-1309; Email: zhaojunwei@henu.edu.cn

Authors

Xin Xu − *Henan Key Laboratory of Polyoxometalate Chemistry, College of Chemistry and Chemical Engineering, Henan University, Kaifeng, Henan 475004, China*

Ruru Meng − *Henan Key Laboratory of Polyoxometalate Chemistry, College of Chemistry and Chemical Engineering, Henan University, Kaifeng, Henan 475004, China*

Changtong Lu − *Henan Key Laboratory of Polyoxometalate Chemistry, College of Chemistry and Chemical Engineering, Henan University, Kaifeng, Henan 475004, China; China Tobacco Henan Industrial Company Ltd., Zhengzhou, Henan 450000, China*

Ling Mei − *Henan Key Laboratory of Polyoxometalate Chemistry, College of Chemistry and Chemical Engineering, Henan University, Kaifeng, Henan 475004, China*

Complete contact information is available at: https://pubs.acs.org/10.1021/acs.inorgchem.9b03620

Notes

The authors declare no competing financial interest.

■ ACKNOWLEDGMENTS

This work was supported by the National Natural Science Foundation of China (21671054, 21871077, 21571048, and 21771052), the Program for Innovation Teams in Science and Technology in Universities of Henan Province (20IRTSTHN004), the Program of First-Class Discipline Cultivation Project of Henan University (2019YLZDYJ02), and the Program for National Innovative Experimental Training for College Students (201910475034).

■ REFERENCES

(1) Parrot, A.; Bernard, A.; Jacquart, A.; Serapian, S. A.; Bo, C.; Derat, E.; Oms, O.; Dolbecq, A.; Proust, A.; Metivier, R.; Mialane, P.; Izzet, G. Photochromism and dual-color fluorescence in a polyoxometalate benzospiropyran molecular switch. *Angew. Chem., Int. Ed.* **2017**, *56*, 4872−4876.

(2) Zheng, Q.; Vila-Nadal, L.; Lang, Z.; Chen, J. J.; Long, D. L.; Mathieson, J. S.; Poblet, J. M.; Cronin, L. Self-sorting of heteroanions in the assembly of cross-shaped polyoxometalate clusters. *J. Am. Chem. Soc.* **2018**, *140*, 2595−2601.

(3) Blazevic, A.; Rompel, A. The Anderson−Evans polyoxometalate: from inorganic building blocks via hybrid organic−inorganic structures to tomorrows "bio-POM. *Coord. Chem. Rev.* **2016**, *307*, 42−64.

(4) Hou, X. S.; Zhu, G. L.; Ren, L. J.; Huang, Z. H.; Zhang, R. B.; Ungar, G.; Yan, L. T.; Wang, W. Mesoscale graphene-like honeycomb mono- and multilayers constructed via self-assembly of coclusters. *J. Am. Chem. Soc.* **2018**, *140*, 1805−1811.

(5) Blazevic, A.; Rompel, A. The Anderson−Evans polyoxometalate: from inorganic building blocks via hybrid organic−inorganic structures to tomorrows "bio-POM. *Coord. Chem. Rev.* **2016**, *307*, 42−64.

(6) Cheng, W.; Shen, F.-C.; Xue, Y.-s.; Luo, X.; Fang, M.; Lan, Y.-Q.; Xu, Y. A pair of rare three-dimensional chiral polyoxometalate-based metal- organic framework enantiomers featuring superior performance as the anode of lithium-ion battery. *ACS Appl. Energy Mater.* **2018**, *1*, 4931−4938.

(7) Yang, P.; Zhao, W.; Shkurenko, A.; Belmabkhout, Y.; Eddaoudi, M.; Dong, X.; Alshareef, H. N.; Khashab, N. M. Polyoxometalate -cyclodextrin metal-organic frameworks: from tunable structure to customized storage functionality. *J. Am. Chem. Soc.* **2019**, *141*, 1847−1851.

(8) Gao, J.; Yan, J.; Beeg, S.; Long, D.-L.; Cronin, L. One-pot versus sequential reactions in the self-assembly of gigantic nanoscale polyoxotungstates. *J. Am. Chem. Soc.* **2013**, *135*, 1796−1805.

(9) Miras, H. N.; Yan, J.; Long, D. L.; Cronin, L. Engineering polyoxometalates with emergent properties. *Chem. Soc. Rev.* **2012**, *41*, 7403−7430.

(10) Artetxe, B. Systematic studies on 3d- and 4f-metal containing polyoxometalates suitable for organic derivatization. *ChemistryOpen* **2016**, *5*, 261−266.

(11) Liu, H.; Qin, C.; Wei, Y.-G.; Xu, L.; Gao, G.-G.; Li, F.-Y.; Qu, X.-S. Copper-complex-linked polytungsto-bismuthate (-antimonite) chain containing sandwich Cu(II) ions partially modified with imidazole ligand. *Inorg. Chem.* **2008**, *47*, 4166−4172.

(12) Raula, M.; Gan Or, G.; Saganovich, M.; Zeiri, O.; Wang, Y.; Chierotti, M. R.; Gobetto, R.; Weinstock, I. A. Polyoxometalate complexes of anatase-titanium dioxide cores in water. *Angew. Chem., Int. Ed.* **2015**, *54*, 12416−12421.

(13) Mizuno, N.; Yamaguchi, K.; Kamata, K. C. Epoxidation of olefins with hydrogen peroxide catalyzed by polyoxometalates. *Coord. Chem. Rev.* **2005**, *249*, 1944−1956.

(14) Ritchie, C.; Moore, E. G.; Speldrich, M.; Kögerler, P.; Boskovic, C. Terbium polyoxometalate organic complexes: correlation of structure with luminescence properties. *Angew. Chem., Int. Ed.* **2010**, *49*, 7702−7871.

https://dx.doi.org/10.1021/acs.inorgchem.9b03620
Inorg. Chem. 2020, 59, 3954−3963

(15) Zhao, J. W.; Li, Y. Z.; Chen, L. J.; Yang, G. Y. Research progress on polyoxometalate-based transition-metal−rare-earth heterometallic derived materials: synthetic strategies, structural overview and functional applications. *Chem. Commun.* **2016**, *52*, 4418−4445.
(16) Liu, J. C.; Luo, J.; Han, Q.; Cao, J.; Chen, L. J.; Song, Y.; Zhao, J. W. Coexistence of long-range ferromagnetic ordering and spin-glass behavior observed in the first inorganic−organic hybrid 1-D oxalate-bridging nona-Mn^{II} sandwiched tungstoantimonate chain. *J. Mater. Chem. C* **2017**, *5*, 2043−2055.
(17) Shang, S. X.; Lin, Z. G.; Yin, A. X.; Yang, S.; Chi, Y. N.; Wang, Y.; Dong, J.; Liu, B.; Zhen, N.; Hill, C. L.; Hu, C. W. Self-assembly of Ln(III)-containing tungstotellurates(VI): correlation of structure and photoluminescence. *Inorg. Chem.* **2018**, *57*, 8831−8840.
(18) Li, Y.; Li, H.; Jiang, J.; Chen, L.; Zhao, J. Three types of distinguishing L-alanine-decorated and rare-earth-incorporated arsenotungstate hybrids prepared in a facile one-step assembly strategy. *Inorg. Chem.* **2019**, *58*, 3479−3491.
(19) Li, Z.; Li, X.-X.; Yang, T.; Cai, Z.-W.; Zheng, S.-T. Four-shell polyoxometalates featuring high-nuclearity Ln_{26} clusters: structural transformations of nanoclusters into frameworks triggered by transition-metal ions. *Angew. Chem., Int. Ed.* **2017**, *56*, 2664−2669.
(20) Wang, Y.-J.; Wu, S.-Y.; Sun, Y.-Q.; Li, X.-X.; Zheng, S.-T. Octahedron-shaped three-shell Ln_{14}-substituted polyoxotungstogermanates encapsulating a W_4O_{15} cluster: luminescence and frequency dependent magnetic properties. *Chem. Commun.* **2019**, *55*, 2857−2860.
(21) Bassil, B. S.; Dickman, M. H.; Römer, I.; von der Kammer, B.; Kortz, U. The tungstogermanate $[Ce_{20}Ge_{10}W_{100}O_{376}(OH)_4(H_2O)_{30}]_{56}$: a polyoxometalate containing 20 cerium(III) atoms. *Angew. Chem., Int. Ed.* **2007**, *46*, 6192−6195.
(22) Wassermann, K.; Dickman, M. H.; Pope, M. T. Self-assembly of supramolecular polyoxometalates: the compact, water-soluble heteropolytungstate anion $[As^{III}_{12}Ce^{III}_{16}(H_2O)_{36}W_{148}O_{524}]^{76-}$. *Angew. Chem., Int. Ed.* **1997**, *36*, 1445−1448.
(23) Zheng, X.-Y.; Wang, S.-Q.; Tang, W.; Zhuang, G.-L.; Kong, X.-J.; Ren, Y.-P.; Long, L.-S.; Zheng, L.-S. Two nanosized 3d-4f clusters featuring four Ln_6 octahedra encapsulating a Zn_4 tetrahedron. *Chem. Commun.* **2015**, *51*, 10687−10690.
(24) Zang, H. Y.; Miras, H. N.; Yan, J.; Long, D.-L.; Cronin, L. Assembly and autochirogenesis of a chiral inorganic polythioanion mobius strip via symmetry breaking. *J. Am. Chem. Soc.* **2012**, *134*, 11376−11379.
(25) Cai, J.; Zheng, X.-Y.; Xie, J.; Yan, Z.-H.; Kong, X.-J.; Ren, Y.-P; Long, L.-S.; Zheng, L.-S. Anion-dependent assembly of heterometallic 3d-4f clusters based on a lacunary polyoxometalate. *Inorg. Chem.* **2017**, *56*, 8439−8445.
(26) Ibrahim, M.; Mal, S. S.; Bassil, B. S.; Banerjee, A.; Kortz, U. yttrium(III)-containing tungstoantimonate(III) stabilized by tetrahedral WO_4^{2-} capping unit, $[\{Y(\alpha\text{-}SbW_9O_{31}(OH)_2)(CH_3COO)(H_2O)\}_3(WO_4)]^{17-}$. *Inorg. Chem.* **2011**, *50*, 956−960.
(27) Liang, Z.; Zhang, L.; Li, Y.; Ma, P.; Niu, J.; Wang, J. Two novel heteropolyniobates using TeO^{32-} as template and linker. *Inorg. Chem.* **2019**, *58*, 27−30.
(28) Li, X.-X.; Fang, W.-H.; Zhao, J.-W.; Yang, G.-Y. The first 3-connected $SrSi_2$-type 3D chiral framework constructed from $\{Ni_6PW_9\}$ building units. *Chem. - Eur. J.* **2015**, *21*, 2315−2318.
(29) Chen, Y. H.; Sun, L. H.; Chang, S. Z.; Chen, L. J.; Zhao, J. W. Synergistic effect between different coordination geometries of lanthanides and various coordination modes of 2-picolinic acid ligands tuning three types of rare 3d-4f heterometallic tungstoantimonates. *Inorg. Chem.* **2018**, *57*, 15079−15092.
(30) Luo, X.-M.; Li, N.-F.; Hu, Z.-B.; Cao, J.-P.; Cui, C.-H.; Lin, Q.-F.; Xu, Y. Polyoxometalate-based well-defined rodlike structural multifunctional materials: synthesis, structure, and properties. *Inorg. Chem.* **2019**, *58*, 2463−2470.
(31) Han, Q.; Liu, J.-C.; Wen, Y.; Chen, L.-J.; Zhao, J.-W.; Yang, G.-Y. Tellurotungstate-based organotin-rare-earth heterometallic hybrids with four organic components. *Inorg. Chem.* **2017**, *56*, 7257−7269.
(32) An, H.; Han, Z.; Xu, T. Three-dimensional architectures based on lanthanide-substituted double-Keggin-type polyoxometalates and lanthanide cations or lanthanide-organic complexes. *Inorg. Chem.* **2010**, *49*, 11403−11414.
(33) Nohra, B.; Mialane, P.; Dolbecq, A.; Rivière, E.; Marrot, J.; Sécheresse, F. Heterometallic 3d−4f cubane clusters inserted in polyoxometalate matrices. *Chem. Commun.* **2009**, *40*, 2703−2705.
(34) Reinoso, S. Heterometallic 3d-4f polyoxometalates: still an incipient field. *Dalton Trans.* **2011**, *40*, 6610−6615.
(35) Chen, W. C.; Jiao, C.-Q.; Wang, X.-L.; Shao, K. Z.; Su, Z.-M. Self-assembly of nanoscale lanthanoid-containing selenotungstates: synthesis, structures, and magnetic studies. *Inorg. Chem.* **2019**, *58*, 12895−12904.
(36) Xue, G.; Vaissermann, J.; Gouzerh, P. Cerium(III) complexes with lacunary polyoxotungstates. Synthesis and structural characterization of a novel heteropolyoxotungstate based on *a*-$[SbW_9O_{33}]^{9-}$ units. *J. Cluster Sci.* **2002**, *13*, 409−421.
(37) Song, Y.-F.; Cronin, L. Postsynthetic covalent modification of metal−organic framework (MOF) materials. *Angew. Chem., Int. Ed.* **2008**, *47*, 4635−4637.
(38) Li, H. L.; Liu, Y. J.; Liu, J. L.; Chen, L. J.; Zhao, J. W.; Yang, G. Y. Structural transformation from dimerization to tetramerization of serine-decorated rare-earth-incorporated arsenotungstates induced by the usage of rare-earth salts. *Chem. - Eur. J.* **2017**, *23*, 2673−2689.
(39) Wang, J.; Liang, Y. F.; Ma, P. T.; Zhang, D. D.; Niu, J. Y.; Wang, J. P. Ligand-controlled formation of covalently modified antimonio-molybdates and their photochromic properties. *CrystEngComm* **2017**, *19*, 207−213.
(40) Almeida Paz, F. A.; Klinowski, J.; Vilela, S. M. F.; Tome, J. P. C.; Cavaleiro, J. A. S.; Rocha, J. Ligand design for functional metal-organic frameworks. *Chem. Soc. Rev.* **2012**, *41*, 1088−1110.
(41) Eliseeva, S. V.; Bunzli, J.-C. G. Lanthanide luminescence for functional materials and bio-sciences. *Chem. Soc. Rev.* **2010**, *39*, 189−227.
(42) Yamase, T. Photo- and electrochromism of polyoxometalates and related materials. *Chem. Rev.* **1998**, *98*, 307.
(43) Kang, F. W.; Sun, G. H.; Wang, A. W.; Xiao, X. F.; Li, Y. Y.; Lu, J.; Huang, B. L. Multicolor tuning and temperature-triggered anomalous Eu^{3+}- related photoemission enhancement via interplay of accelerated energy transfer and release of defect-trapped electrons in the Tb^{3+}, Eu^{3+}-doped strontium-aluminum chlorites. *ACS Appl. Mater. Interfaces* **2018**, *10*, 36157−36170.
(44) Zhou, X.; Wang, H.; Jiang, S.; Xiang, G.; Tang, X.; Luo, X.; Li, L.; Zhou, X. Multifunctional luminescent material Eu(III) and Tb(III) complexes with pyridine-3,5-dicarboxylic acid linker: crystal structures, tunable emission, energy transfer, and temperature sensing. *Inorg. Chem.* **2019**, *58*, 3780−3788.
(45) Ritchie, C.; Baslon, V.; Moore, E. G.; Reber, C.; Boskovic, C. Sensitization of lanthanoid luminescence by organic and inorganic ligands in lanthanoid-organic-polyoxometalates. *Inorg. Chem.* **2012**, *51*, 1142−1151.
(46) Wu, H.; Yan, B.; Li, H.; Singh, V.; Ma, P.; Niu, J.; Wang, J. Enhanced photostability luminescent properties of Er^{3+}-doped near-white-emitting $Dy_xEr_{(1-x)}$-POM derivatives. *Inorg. Chem.* **2018**, *57*, 7665−7675.
(47) Horrocks, W. DeW., Jr.; Sudnick, D. R. Lanthanide ion probes of structure in biology. laser-induced luminescence decay constants provide a direct measure of the number of metal-coordinated water molecules. *J. Am. Chem. Soc.* **1979**, *101*, 334−340.
(48) Pavani, K.; Kumar, J. S.; Sasikala, T.; Jamalaiah, B. C.; Seo, H. J.; Moorthy, L. R. Luminescent characteristics of Dy^{3+} doped strontium magnesium aluminate phosphor for white LEDs. *Mater. Chem. Phys.* **2011**, *129*, 292−295.
(49) Quici, S.; Marzanni, G.; Forni, A.; Accorsi, G.; Barigelletti, F. New lanthanide complexes for sensitized visible and near-IR light emission: synthesis, ^1H NMR, and X-Ray structural investigation and photophysical properties. *Inorg. Chem.* **2004**, *43*, 1294−1301.
(50) Xu, X.; Chen, Y. H.; Zhang, Y.; Liu, Y. F.; Chen, L. J.; Zhao, J. W. Rare-earth and antimony-oxo clusters simultaneously connecting

https://dx.doi.org/10.1021/acs.inorgchem.9b03620
Inorg. Chem. 2020, 59, 3954−3963

antimonotungstates comprising divacant and tetravacant Keggin fragments. *Inorg. Chem.* **2019**, *58*, 11636−11648.
(51) Zhang, Q. W.; Li, D. F.; Li, X.; White, P. B.; Mecinović, J. Ma X.; Ma, X.; Ågren, H.; Nolte, R. J. M.; Tian, H. Multicolor photoluminescence including white-light emission by a single host-guest complex. *J. Am. Chem. Soc.* **2016**, *138*, 13541−13550.
(52) Artetxe, B.; Reinoso, S.; San Felices, L.; Lezama, L.; Gutierrez-Zorrilla, J. M.; García, J. A.; Galan-Mascaros, J. R.; Haider, A.; Kortz, U.; Vicent, C. Cation-directed dimeric versus tetrameric assemblies of lanthanide-stabilized dilacunary Keggin tungstogermanates. *Chem. - Eur. J.* **2014**, *20*, 12144−12156.
(53) Artetxe, B.; Reinoso, S.; San Felices, L.; Gutierrez-Zorrilla, J. M.; García, J. A.; Haso, F.; Liu, T.; Vicent, C. Crown-shaped tungstogermanates as solvent-controlled dual systems in the formation of vesicle-like assemblies. *Chem. - Eur. J.* **2015**, *21*, 7736−7745.
(54) Yamase, T.; Sugeta, M. Charge-transfer photoluminescence of polyoxotungstates. *J. Chem. Soc., Dalton Trans.* **1993**, 759−765.
(55) Banerjee, A. K.; Mukhopadhyay, A. K.; Mukherjee, R. K.; Chowdhury, M. $^7F_0$-$^5D_1$ transition in Eu^{3+}-hexakisantipyrenetriiodide single crystal. A magnetic dipole transition. *Chem. Phys. Lett.* **1979**, *67*, 418−419.
(56) Li, H.; Zhao, R.; Jia, Y.; Sun, W.; Fu, J.; Jiang, L.; Zhang, S.; Pang, R.; Li, C. $Sr_{1.7}Zn_{0.3}CeO_4$: Eu^{3+} novel red-emitting phosphors: synthesis and photoluminescence properties. *ACS Appl. Mater. Interfaces* **2014**, *6*, 3163−3169.
(57) Wang, J. W.; Chang, Y. M.; Chang, H. C.; Lin, S. H.; Huang, L. C. L; Kong, X. L.; Kang, M. W. Local structure dependence of the charge transfer band in nanocrystalline Y_2O_3:Eu^{3+}. *Chem. Phys. Lett.* **2005**, *405*, 314−317.
(58) Wei, Z.; Sun, L.; Liao, C.; Yin, J.; Jiang, X.; Yan, C.; Lu, S. Size-dependent chromaticity in YBO_3:Eu nanocrystals: correlation with microstructure and site symmetry. *J. Phys. Chem. B* **2002**, *106*, 10610−10617.
(59) Carrasco, I.; Piccinelli, F.; Romet, I.; Nagirnyi, V.; Bettinelli, M. Competition between energy transfer and energy migration processes in neat and Eu^{3+}-Doped $TbPO_4$. *J. Phys. Chem. C* **2018**, *122*, 6858−6864.
(60) Zmojda, J.; Kochanowicz, M.; Miluski, P.; Dorosz, J.; Pisarska, J.; Pisarski, W. A.; Dorosz, D. Investigation of upconversion luminescence in antimony-germanate double-clad two cores optical fiber co-doped with Yb^{3+}/Tm^{3+} and Yb^{3+}/Ho^{3+} ions. *J. Lumin.* **2016**, *170*, 795−800.
(61) Zhang, Y.; Gong, W.; Yu, J.; Lin, Y.; Ning, G. Tunable white-light emission via energy transfer in single-phase $LiGd(WO_4)_2$:RE^{3+} (RE = Tm, Tb, Dy, Eu) phosphors for UV-excited WLEDs. *RSC Adv.* **2015**, *5*, 96272−96280.
(62) Liu, Y.; Liu, G. X.; Wang, J. X.; Dong, X. T.; Yu, W. S. Single-component and warm-white-emitting phosphor $NaGd(WO_4)_2$:Tm^{3+}, Dy^{3+}, Eu^{3+}: synthesis, luminescence, energy transfer, and tunable color. *Inorg. Chem.* **2014**, *53*, 11457−11466.
(63) Chung, J. H.; Ryu, J. H.; Mhin, S. W.; Kim, K. M.; Shim, K. B. Controllable white upconversion luminescence in Ho^{3+}/Tm^{3+}/Yb^{3+} co-doped $CaMoO_4$. *J. Mater. Chem.* **2012**, *22*, 3997−4002.
(64) Yu, Y.; Zheng, Y.; Qin, F.; Liu, L.; Zheng, C.; Chen, G.; Zhang, Z.; Cao, W. Influence of Yb^{3+} concentration on upconversion luminescence of Ho^{3+}. *Opt. Commun.* **2011**, *284*, 1053−1056.
(65) Dexter, D. L.; Schulman, J. A. Theory of concentration quenching in inorganic phosphors. *J. Chem. Phys.* **1954**, *22*, 1063−1070.
(66) Kapogiannatou, A.; Paronis, E.; Paschidis, K.; Polissidis, A.; Kostomitsopoulos, N. G. Effect of light colour temperature and intensity on the behaviour of male C57CL/6J mice. *Appl. Anim. Behav. Sci.* **2016**, *184*, 135−140.
(67) Wang, Q.; Xu, H. S.; Zhang, F. Z.; Wang, Z. H. Influence of color temperature on comfort and preference for LED indoor lighting. *Optik* **2017**, *129*, 21−29.
(68) Zhang, Y.; Gong, W.; Yu, J.; Pang, H.; Song, Q.; Ning, G. A new single -phase white-light-emitting $CaWO_4$:Dy^{3+} phosphor: synthesis, luminescence and energy transfer. *RSC Adv.* **2015**, *5*, 62527−62533.
(69) McCamy, C. S. Correlated color temperature as an explicit function of chromaticity coordinates. *Color Res. Appl.* **1992**, *17*, 142−144.
(70) Suresh Kumar, J.; Pavani, K.; Mohan Babu, A.; Kumar Giri, N.; Rai, S.B.; Moorthy, L. R. Fluorescence characteristics of Dy^{3+} ions in calcium fluoroborate glasses. *J. Lumin.* **2010**, *130*, 1916−1923.
(71) Du, J.; Huang, L.; Zhu, L. Absorption cross sections of surface-adsorbed H_2O in the 295−370 nm region and heterogeneous nucleation of H_2O on fused silica surfaces. *J. Phys. Chem. A* **2013**, *117*, 8907−8914.
(72) Ma, Z.; Li, F.; Qi, G.; Wang, L.; Liu, C.; Wang, K.; Xiao, G.; Zou, B. Structural stability and optical properties of two-dimensional perovskite-like $CsPb_2Br_5$ microplates in response to pressure. *Nanoscale* **2019**, *11*, 820−825.
(73) Yan, B.; Lin, L.; Wu, J.; Lei, F. Photoluminescence of rare earth phosphors $Na_{0.5}Gd_{0.5}WO_4$: RE^{3+} and $Na_{0.5}Gd_{0.5}(Mo_{0.75}W_{0.25})O_4$: RE^{3+} (RE = Eu, Sm, Dy). *J. Fluoresc.* **2011**, *21*, 203−211.

https://dx.doi.org/10.1021/acs.inorgchem.9b03620
Inorg. Chem. 2020, 59, 3954−3963